Nuclear Science and Techniques (2025) 36:88
https://doi.org/10.1007/s41365-025-01654-y

Study of the elastic scattering effects of a slowing-down model on D–T neutron porosity logging

Shao-Heng Zhou[1,2,3] · Ying-Long Tao[3] · Bo Chang[3] · Li-Juan Hao[3,4] · Jie-Qiong Jiang[1,5] · Ya-Zhou Li[3,5,6] · Fang Wang[3,5,6] · Quan Gan[3,6] · FDS Consortium

Received: 17 January 2024 / Revised: 9 April 2024 / Accepted: 8 May 2024 / Published online: 20 March 2025

Abstract

The application of a controllable neutron source for measuring formation porosity in the advancement of nuclear logging has garnered increased attention. The existing porosity algorithm, which is based on the thermal neutron counting ratio, exhibits lower sensitivity in high-porosity regions. To enhance the sensitivity, the effects of elastic and inelastic scattering, which influence the slowing-down of fast neutrons, were theoretically analyzed, and a slowing-down model of fast neutrons was created. Based on this model, a density correction porosity algorithm was proposed based on the relationship between density, thermal neutron counting ratio, and porosity. Finally, the super multifunctional calculation program for nuclear design and safety evaluation (TopMC/SuperMC) was used to create a simulation model for porosity logging, and its applicability was examined. The results demonstrated that the relative error between the calculated and actual porosities was less than 1%, and the influence of deviation in the density measurement was less than 2%. Therefore, the proposed density correction algorithm based on the slowing-down model of fast neutrons can effectively improve the sensitivity in the high-porosity region. This study is expected to serve as a reference for the application of neutron porosity measurements with D–T neutron sources.

Keywords D–T neutron source · Slowing-down model · Elastic scattering · Neutron porosity

1 Introduction

Neutron porosity logging is a conventional geophysical measurement method used to determine the formation porosity. The americium–beryllium (Am–Be) source is commonly used for conventional porosity measurements. However, they pose potential risks to safety, health, and the environment [1–4]. Researchers have studied substitution chemical sources with deuterium–deuterium (D–D) neutrons [5–7]. However, the neutron yield of D–D neutron sources is relatively low, which restricts their application [8, 9].

In 2005, the oilfield services company Schlumberger (now SLB) began using a deuterium–tritium (D–T) neutron source for compensated thermal neutron porosity logging [10]. Compared to the chemical source, the D–T neutron source has a higher neutron yield, higher neutron energy of 14 MeV, and a longer slowing-down length of the neutron; thus, D–T neutron logging can detect more thermal neutrons and has a higher detection accuracy.

Nevertheless, neutron slowing-down is facilitated by inelastic scattering owing to the higher energy of neutrons.

This work was partly supported by the Anhui Provincial Major Science and Technology Project (No. 201903c08020003) and the Taishan industrial Experts Program.

✉ Li-Juan Hao
lijuan.hao@fds.org.cn

1 Hefei Institutes of Physical Science, Chinese Academy of Sciences, Hefei 230031, China

2 University of Science and Technology of China, Hefei 230026, China

3 International Academy of Neutron Science, Qingdao 266199, China

4 Thinking Neutron Technology Co., Ltd., Hefei 230031, China

5 Institute of Nuclear Science and Technology, Shandong University, Jinan 250061, China

6 Shandong Key Laboratory of Neutron Science and Technology, Qingdao 266199, China

Consequently, the D–T neutron recording exhibits reduced sensitivity to porosity compared to the chemical source [11, 12], as measured by the conventional neutron porosity interpretation model founded on the Am–Be source [13–15].

To overcome this problem, various density correction methods have been proposed to improve the porosity sensitivity of D–T neutron logging. The near and far thermal neutron counts were corrected using the density correction function, and the modified thermal neutron counting ratio was considered to be only associated with the hydrogen-containing index [16]. Further, the density correction methods were summarized to modify the thermal neutron counting ratio and studied by MC simulation [17]. The relationship of slowing-down length of neutrons between the formation density and hydrogen index was deduced and numerically simulated [18]. Based on data from the standard calibration experiment and actual logging [19, 20], it was verified that the density correction results were consistent with the isotopic neutron source.

In addition, the slowing-down length of the D–T neutron source can be converted into that of the Am–Be source. One method involves the relationship between the neutron slowing-down length, capturing of the cross section, and density to predict the counting ratio [21]. The second involves the combination of the two-group diffusion theory with the formation density, reaction cross section, and neutron slowing-down length [22].

In these studies, the slowing-down length is written as $L_s^2 = L^2_{E_0-E_1} + L^2_{E_1-E_t}$, where $L_{E_0-E_1}$ is the slowing-down length for neutrons from energy $E_0 = 14$ MeV to E_1, and $L_{E_1-E_t}$ is the slowing-down length for neutrons from energy E_1 to E_t of thermal neutron. The corresponding correction methods are based on the assumption that the slowing-down length is determined by the inelastic scattering from E_0 to E_1 and the contribution of elastic scattering is ignored.

The slowing-down of neutrons is the result of both elastic and inelastic scattering. At high porosity, because of the higher hydrogen content, the free mean path of elastic scattering is short [23, 24] and $L_{E_0-E_1}$ is dominated by inelastic scattering. At low porosity, elastic scattering cannot be ignored because of the long free mean path of the elastic scattering of D–T neutrons for $L_{E_0-E_1}$ that are primarily contributed by C, O, and Ca. Ignoring this results in measurement deviations in porosity logging at low porosities. To improve the accuracy of D–T neutron porosity logging, a neutron slowing-down model of the D–T source is presented in Sect. 2, which considers elastic scattering in the entire process. In this model, both elastic and inelastic scattering are considered for neutron slowdown. Based on this model, an algorithm for porosity density correction based on the relationship between the density and porosity is developed in Sect. 3. Finally, the effectiveness of the proposed method is verified using a multifunctional calculation program for nuclear design and safety evaluation (TopMC/SuperMC) [25].

2 Theoretical analysis

2.1 Distribution of the thermal neutron

Based on the two-group diffusion theory, the distribution of the thermal neutron flux density for a fast neutron point source in an infinite uniform medium is expressed as [22]

$$\varphi_t(r) = \frac{Q}{4\pi D_t r}\frac{L_t^2}{L_f^2 - L_t^2}\left(e^{-r/L_f} - e^{-r/L_t}\right), \tag{1}$$

where Q is the strength of the fast neutron point source, r is the detector spacing, and D_t, L_f, L_t are the thermal neutron diffusion coefficient, fast neutron slowing-down length, and thermal neutron diffusion length, respectively. In a normal formation, L_f is significantly larger than L_t, and Eq. (1) can be approximated as follows:

$$\varphi_t(r) = \frac{Q}{4\pi D_t r}\frac{L_t^2}{L_f^2 - L_t^2}e^{-r/L_f}. \tag{2}$$

Assuming that the near and far detector spacings are r_s and r_l (as shown in Fig. 1), and the detector efficiencies are η_l and η_s, the detector counting ratios of the near and far detectors are expressed as follows:

$$R_t = \frac{\eta_l r_l}{\eta_s r_s}e^{(r_l - r_s)/L_f}. \tag{3}$$

The detector counting ratio is related to the length of the fast neutron slowing-down length.

In conventional compensated porosity logging, the energy of the neutrons emitted from the Am–Be source is below 5 MeV, and the neutrons are primarily slowed down by elastic

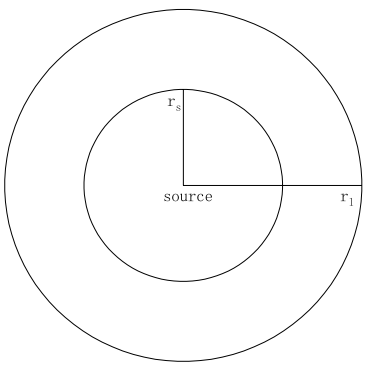

Fig. 1 Model of point source

scattering with hydrogen in the formation. The counting ratio of the thermal neutrons reflects the porosity of the formation. However, the neutron produced by the D–T reaction has an energy of 14 MeV, and neutrons are slowed down by elastic and inelastic reactions with the elements of the formation. Therefore, the porosity of the formation cannot be directly determined by the counting ratio of thermal neutrons.

2.2 The slowing-down model of the fast neutron

In this subsection, a slowing-down model of the D–T neutron is established to investigate the relationship between the slowing-down length L_f and elastic scattering, particularly at low porosity.

According to the diffusion equation [23], the slowing-down length L_f can be expressed as:

$$L_f = \sqrt{\frac{\overline{r^2}}{6}}, \tag{4}$$

where r is the straight-line distance from a D–T neutron slowed down to a thermal neutron. As shown in Fig. 2, the neutron slowing-down process can be calculated using the multigroup calculation method [26].

According to neutronics,

$$\overline{r^2} = \overline{r_1^2} + \overline{r_2^2} + \cdots + \overline{r_n^2} \tag{5}$$

where r_k is the distance traveled by the neutron between the $(k-1)$th and kth scattering with the formation, E_0 is the energy of the D–T neutrons of 14 MeV, and E_t is the energy of the thermal neutrons.

When a neuron slows, there are two types of scattering: elastic and inelastic. In elastic scattering, the neutron strikes the nucleus, and the state of the nucleus remains in the ground state. The process of inelastic scattering is identical to that of elastic scattering except that the nucleus remains in an excited state. Neutrons are slowed by numerous elastic and inelastic scatterings. Therefore, $\overline{r^2}$ in Eq. (5) is expressed as follows:

$$\overline{r^2} = \bar{n}_{in}\overline{r_{in}^2} + \bar{n}_{el}\overline{r_{el}^2} \tag{6}$$

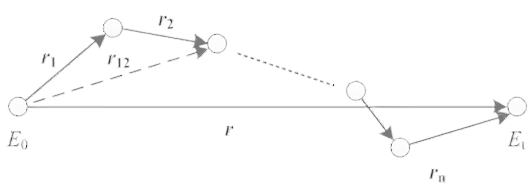

Fig. 2 Neutron slowing-down process

where $\bar{n}_{in}$ and $\bar{n}_{el}$ are the average inelastic and elastic scattering numbers, respectively. Further, $\overline{r_{in}^2}$ and $\overline{r_{el}^2}$ can be expressed as

$$\begin{aligned} \overline{r_{in}^2} &= 2\lambda_{in}^2 = \frac{2}{\Sigma_{in}^2} \\ \overline{r_{el}^2} &= 2\lambda_{el}^2 = \frac{2}{\Sigma_{el}^2} \end{aligned} \tag{7}$$

where λ_{in} and λ_{el} are the inelastic and elastic mean free paths, respectively, and Σ_{in} and Σ_{el} are the macroscopic inelastic and elastic cross sections, respectively. By substituting Eqs. (6) and (7) into Eq. (4), L_f is rewritten as

$$L_f = \sqrt{\frac{\bar{n}_{in}}{3\Sigma_{in}^2} + \frac{\bar{n}_{el}}{3\Sigma_{el}^2}} \tag{8}$$

A neutron slowing-down model was established to obtain $\bar{n}_{in}$ and $\bar{n}_{el}$. In this model, neutrons were slowed by elastic scattering or both elastic and inelastic scattering. To simplify the calculation, it was assumed that inelastic scattering is effective such that the energy of the neutrons fell below E_1, which is the threshold of inelastic scattering, by single inelastic scattering.

We assume that $a = \frac{\Sigma_{in}}{\Sigma_{in}+\Sigma_{el}}$ and $b = \frac{\Sigma_{el}}{\Sigma_{in}+\Sigma_{el}}$ are the probabilities of inelastic and elastic scattering, respectively, and the neutron energy drops to E_1 after i collisions of elastic scattering. When $i = \frac{\ln\left(\frac{E_0}{E_1}\right)}{\zeta}$, ζ is the lethargy of the formation owing to an elastic collision [23].

Based on this assumption, $\bar{n}_{in}$ and $\bar{n}_{el}$ can be obtained as follows:

$$\begin{aligned} \bar{n}_{in} &= a\frac{1-b^i}{1-b} \\ &= \frac{\Sigma_{in}}{\Sigma_{in}+\Sigma_{el}}\frac{1-b^i}{1-b} \\ \bar{n}_{el} &= i + b\frac{1-b^i}{1-b} \\ &= \frac{\ln\left(\frac{E_1}{E_t}\right)}{\zeta} + \frac{\Sigma_{el}}{\Sigma_{in}+\Sigma_{el}}\frac{1-b^i}{1-b} \end{aligned} \tag{9}$$

The above equations indicate that $\bar{n}_{in}$ and $\bar{n}_{el}$ are affected by the Σ_{el}, Σ_{in}, and ζ, which are determined by the nuclides in the formation. Further, $b\frac{1-b^i}{1-b}$ is the average number of elastic scattering during the neutron slowing-down process from the E_0 to the E_1. As the elastic scattering cross section Σ_{el} in the formation is considerably larger than the inelastic scattering cross section Σ_{in}, we have $\frac{1-b^i}{1-b} \approx i = \frac{\ln\left(\frac{E_0}{E_1}\right)}{\zeta}$. By substituting Eq. (9) into Eq. (8), L_f can be rewritten as follows:

$$L_{\mathrm{f}} = \sqrt{\left(L^{\mathrm{in}}_{E_0-E_1}\right)^2 + \left(L^{\mathrm{el}}_{E_0-E_1}\right)^2 + \left(L^{\mathrm{el}}_{E_1-E_{\mathrm{t}}}\right)^2} \tag{10}$$

where $L^{\mathrm{in}}_{E_0-E_1} = \sqrt{\frac{\ln\left(\frac{E_0}{E_1}\right)}{3\zeta\Sigma_{\mathrm{in}}(\Sigma_{\mathrm{in}}+\Sigma_{\mathrm{el}})}}$ is the slowing-down length of the inelastic scattering, $L^{\mathrm{el}}_{E_0-E_1} = \sqrt{\frac{\ln\left(\frac{E_0}{E_1}\right)}{3\zeta\Sigma_{\mathrm{el}}(\Sigma_{\mathrm{in}}+\Sigma_{\mathrm{el}})}}$ is the slowing-down length of the elastic scattering in the neutron slowing-down process from energy E_0 to the E_1 and $L^{\mathrm{el}}_{E_1-E_{\mathrm{t}}} = \sqrt{\frac{\ln\left(\frac{E_1}{E_{\mathrm{t}}}\right)}{3\Sigma^2_{\mathrm{el}}\zeta}}$ is the slowing-down length of the elastic scattering through which the neutron is slowed down from the energy E_1 to E_{t}. Equation (10) shows that the elastic scattering of high-energy neutrons corrects the slowing-down length.

2.3 Slowing-down model of the fast neutron

To analyze the effects of elastic and inelastic scattering on the neutron slowing-down length, Table 1 presents the theoretical calculation results for the slowing-down length of D–T neutrons in limestone with different porosities (0% to 100%). Specifically, the threshold of inelastic scattering was set to 3.6 MeV for limestone [24], and the cross sections for inelastic and elastic scattering attained the one correspond to the neutron energies of 14 MeV and 10 MeV.

When the porosity of the limestone was 0%, there was no water in the limestone; the macroscopic cross section of inelastic scattering was 0.0279 cm^{-1}, and the macroscopic cross section of elastic scattering was 0.3248 cm^{-1} [24]. Therefore, the free path of inelastic scattering was approximately 35 cm, whereas that of elastic scattering was approximately 3 cm. However, the nuclides in limestone are primarily C, H, and Ca. These nuclides have a weaker ability to slow down neutrons, thus resulting in more elastic collisions (about 165 times). This resulted in $\left(L^{\mathrm{el}}_{E_0-E_{\mathrm{t}}}\right)^2 = 525.56\ \mathrm{cm}^2$ and $\left(L^{\mathrm{in}}_{E_0-E_1}\right)^2 = 262.36\ \mathrm{cm}^2$. Thus, the effect of elastic scattering on the slowing-down length exceeded the contribution of inelastic scattering. These factors resulted in a theoretically calculated slowing-down length of the D–T neutrons up to 28 cm. As the amount of water in the limestone increased, the porosity increased. In this situation, the macroscopic cross section of the inelastic scattering decreased slowly; however, the macroscopic cross section of the elastic scattering increased rapidly. In particular, hydrogen, the nuclide with the strongest ability to slow down neutrons, also caused the number of elastic scatterings to decrease rapidly. For example, when the porosity was increased to 10%, the number of elastic scatterings decreased to 43, the elastic scattering free path was 2.0 cm, the number of inelastic scatterings decreased to 0.14, and the inelastic scattering free path was 38 cm. At this point, the contribution of the elastic scattering to the slowing-down length was less than that of the inelastic scattering. When the porosity exceeded 50%, the contribution of elastic scattering was significantly lower than that of inelastic scattering and could be ignored.

When the slowing-down power of the formation is weak, neutrons are more likely to reduce their energy through inelastic scattering; therefore, inelastic scattering occurs more frequently. When the slowing-down power of the formation is enhanced, the neutrons can reduce the energy to below E_1 through a few collisions. Therefore, the probability and amount of inelastic scattering decrease. However, the free path of elastic scattering is small, rendering the contribution of inelastic scattering to the slowing-down length more dominant. Table 1 also indicates the contribution of the elastic scattering of the D–T neutron in the high-energy region (14 MeV to E_1). The variation of the slowing-down length of the elastic scattering in the high-energy region $\left(L^{\mathrm{el}}_{E_0-E_1}\right)^2$ was consistent with the variation of the whole elas-

Table 1 Theoretical calculated parameters of D–T neutron slowing-down length in limestone

Porosity (%)	n_{el}	n_{in}	$\left(L^{\mathrm{in}}_{E_0-E_1}\right)^2$ (cm^2)	$\left(L^{\mathrm{el}}_{E_0-E_1}\right)^2$ (cm^2)	$\left(L^{\mathrm{el}}_{E_1-E_{\mathrm{t}}}\right)^2$ (cm^2)	$\left(L^{\mathrm{el}}_{E_0-E_{\mathrm{t}}}\right)^2$ (cm^2)	$\frac{\left(L^{\mathrm{el}}_{E_0-E_1}\right)^2}{\left(L^{\mathrm{el}}_{E_0-E_{\mathrm{t}}}\right)^2}$ (%)
0	166.33	0.613	262.36	22.54	503.02	525.56	4.29
10	42.76	0.136	66.35	3.42	52.10	22.28	6.42
20	31.70	0.072	40.28	1.43	20.85	7.64	6.54
30	27.55	0.047	30.41	0.79	11.33	3.85	6.75
40	25.38	0.033	25.29	0.50	7.14	2.32	6.90
50	24.05	0.025	22.49	0.35	4.91	1.54	6.49
60	23.14	0.019	20.80	0.26	3.59	55.52	6.16
70	22.49	0.021	20.04	0.20	2.74	12.12	6.52
80	21.99	0.015	19.80	0.16	2.16	5.26	6.65
90	21.61	0.009	20.31	0.13	1.75	2.94	6.80
100	21.30	0.007	21.35	0.10	1.44	1.88	6.91

tic scattering slowing-down length, that is, the slowing-down length of the elastic scattering decreased rapidly as the porosity increased. However, the slowing-down length of the elastic scattering from E_1 to E_t decreased faster than that in the high-energy region.

When the porosity was 0%, the proportion of $(L^{el}_{E_0-E_1})^2$ in the elastic scattering reached approximately 4%, whereas at a porosity of 30%, the proportion of $(L^{el}_{E_0-E_1})^2$ was approximately 7%. Therefore, the contribution of elastic scattering in obtaining more accurate porosity measurements cannot be ignored. Therefore, when addressing the slowing-down length above the inelastic threshold energy, although the contribution of the slowing-down length primarily originates from inelastic scattering, the contribution of elastic scattering cannot be ignored. Otherwise, it affects the accuracy of the porosity measurement.

In the existing D–T neutron porosity logging method, the elastic scattering of the high-energy part is directly ignored, and porosity measurement is directly associated with elastic scattering below the threshold energy. As shown in the table above, although the elastic scattering of high-energy neutrons has a minimal contribution to the slowing-down length during the D–T neutron slowing-down process, it can still cause an error of approximately 4% if ignored. Therefore, if D–T neutrons are used for porosity logging, it is necessary to establish a suitable porosity logging method suitable for the D–T neutron.

3 Density correction porosity algorithm

According to Eq. (3), the thermal neutron counting ratio R_t remains almost unchanged in the high-porosity region because of inelastic scattering [22]. Therefore, the porosity is less sensitive to the thermal neutron counting ratio for the D–T neutron source at high porosity. To enhance the sensitivity of porosity, a density correction method based on Eq. (11) is introduced in this section. By combining Eqs. (9) and (10), the slowing-down length can be written as follows:

$$L_f = \sqrt{\frac{\ln\left(\frac{E_0}{E_1}\right)\Sigma_{in}}{3\zeta\Sigma_{in}^2(\Sigma_{in}+\Sigma_{el})} + \frac{\ln\left(\frac{E_1}{E_t}\right)}{3\zeta\Sigma_{el}^2} + \frac{\ln\left(\frac{E_0}{E_1}\right)\Sigma_{el}}{3\zeta\Sigma_{el}^2(\Sigma_{in}+\Sigma_{el})}} \tag{11}$$

Equation (11) shows that L_f is correlated with the macroscopic cross section of elastic and inelastic scattering, and the contribution of elastic scattering to the slowing-down length is divided into terms above and below E_1. This shows that elastic scattering cannot be ignored compared with inelastic scattering, particularly for cases with low porosity.

If the pore medium is pure water, the relationship between formation density and porosity can be described as follows:

$$\rho = \phi + (1-\phi)\rho_b \tag{12}$$

where ρ is the density of the formation in units g/cm^3, ρ_b is the density of the stone, and ϕ is the porosity.

The lethargy of the formation by an elastic collision ζ can be expressed as

$$\begin{aligned}\zeta &= \frac{\sum_i^n \zeta_i N_i \sigma_{el}^i}{\sum_i^n N_i \sigma_{el}^i} \\ &= \frac{\zeta_b N_b \sigma_{el}^b + \zeta_H N_H \sigma_{el}^H + \zeta_O N_O \sigma_{el}^O}{\Sigma_{el}}\end{aligned} \tag{13}$$

where ζ_b, ζ_O, and ζ_H are the lethargies of the stone, oxygen, and hydrogen, respectively, and ζ_i, N_i, and σ_{el}^i are the lethargy, nucleon density, and microscopic elastic scattering cross section of the ith nuclide in the formation, According to Eqs. (12) and (13), the macroscopic cross section can be rewritten as a function of the porosity and density of the formation.

$$\begin{aligned}\Sigma_{in} &= N_A\left[\frac{\rho_b\sigma_{in}^b}{M_b}(1-\phi) + \frac{\sigma_{in}^O}{18}\phi\right] \\ &= N_A\left[\frac{\rho_b\sigma_{in}^b}{M_b}\frac{1-\rho}{1-\rho_b} + \frac{\sigma_{in}^O}{18}\frac{\rho-\rho_b}{1-\rho_b}\right] \\ \Sigma_{el} &= N_A\left[\frac{\rho_b\sigma_{el}^b}{M_b}(1-\phi) + \frac{\sigma_{el}^O + 2\sigma_{el}^H}{18}\phi\right] \\ \zeta\Sigma_{el} &= N_A\left[\frac{\rho_b\zeta_b\sigma_{el}^b}{M_b}(1-\phi) + \frac{\zeta_O\sigma_{el}^O + 2\zeta_H\sigma_{el}^H}{18}\phi\right]\end{aligned} \tag{14}$$

where N_A is the Avogadro constant, ρ_b is the density of the stone, M_b is the molecular weight of the stone, and $\sigma_{in/el}^b$, $\sigma_{in/el}^O$, and σ_{el}^H are the corresponding inelastic/elastic cross sections of the stone, oxygen, and hydrogen, respectively. As evident, Σ_{in} exhibits a linear relationship with ρ and Σ_{el} and $\zeta\Sigma_{el}$ have a linear relationship with ϕ.

Substituting Eqs. (11) and (14) into Eq. (3), the relationship between the porosity ϕ, density ρ and ratio R_t is obtained as follows:

$$\begin{aligned}L_f &= \left(\frac{r_1 - r_s}{\ln(\frac{\eta_s r_s}{\eta_l r_l}R_t)}\right)^2 \\ &= \frac{\ln(\frac{E_0}{E_1})\Sigma_{el} + \ln(\frac{E_1}{E_t})\Sigma_{in}}{3\zeta\Sigma_{el}\Sigma_{in}\Sigma_{el}}\end{aligned} \tag{15}$$

The equation above is a second-order function of ϕ, and the root can be obtained as follows:

$$\phi = \frac{1}{2}\left(\sqrt{Y^2 - 4Z} - Y\right) \tag{16}$$

In Eq. (16), $Z = C + D \times f\left(R_t\right) \times (g(\rho) + E)$ and $Y = A + B \times f\left(R_t\right) \times g(\rho)$, where $f(R_t)$ is a function of second-order polynomial with $\ln(R_t)$, and $g(\rho)$ has a linear relationship with $\frac{1}{\rho}$. The constants A, B, C, D, E are calibration factors related to the lithology of the formation and the source distances of the detectors, and can be calibrated in actual logging.

Equation (16) shows that there exists a complex relationship between porosity, density, and thermal counting ratio. In general, the porosity cannot be simply written as the product of $f(R_t)$ and $g(\rho)$. Therefore, the product of $f(R_t)$ and $g(\rho)$ results in deviations in the D–T neutron porosity logging.

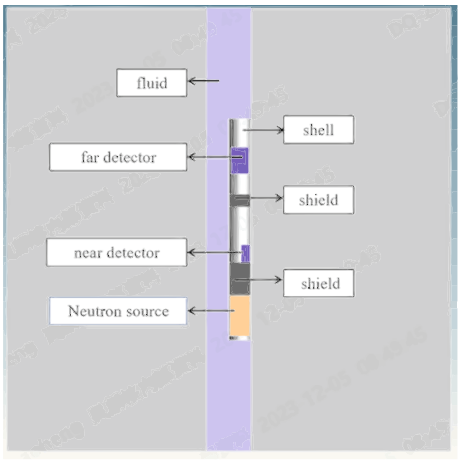

Fig. 3 (Color online) Model of the instrument and the formation

4 Simulation and analysis

Monte Carlo numerical simulation technology is widely used in nuclear logging [27–32]. It can effectively, accurately, and reliably simulate the propagation and interaction of particles in a formation, thereby predicting various nuclear logging parameters. This is of great significance for optimizing logging design, improving logging interpretation accuracy, and other aspects. To verify the validity of Eq. (16), a porosity logging instrument model and a standard well model with TopMC/SuperMC were constructed. Consequently, the application of neutron porosity is investigated in this section.

4.1 Monte Carlo simulation

To verify the performance of the proposed algorithm, TopMC/SuperMC was used to build the tool model and simulate D–T neutron porosity logging.

With reference to the NeoScope logging tool of Schlumberger, and considering the actual situation of the instrument, including the size of the instrument, detector size, and thickness of the shield layer, the instrument design is shown in Fig. 3. A neutron porosity logging instrument was developed using a D–T neutron source, two ^{3}He neutron detectors, and two shields. The neutron yield of the D–T neutron source was set as isotopic, and the near and far source-to-detector spacings were 35 cm and 70 cm. To reduce the direct measurement interference from the neutron source, neutron shields were placed between the neutron source and the near detector, as well as between the near and far detectors, which were made of tungsten alloy. The borehole, with a diameter of 20 cm, was filled with fresh water and surrounded by limestone rocks of varying porosities with a diameter and height of 200 cm. The instrument was compressed against the borehole wall, and the limestone density was 2.703 g/cm^3.

Based on the calculation model shown in Fig. 3, the thermal neutron counts were simulated for different porosities. By combining the simulated results with the least-squares method, the coefficients in Eq. (16) are determined as follows:

$$\phi = \frac{1}{2}\left(\sqrt{Y^2 - 4Z} - Y\right) \tag{17}$$

In Eq. (17), $Z = 0.1431 \times f\left(R_t\right) \times (g(\rho) + 0.092) - 0.0046$ and $Y = 4.6069 - 0.9431 \times f\left(R_t\right) \times g(\rho)$.

4.2 Verification of the algorithm

According to the algorithm of Eq. (17), the D–T neutron porosity logging was simulated with limestone porosity of 0.1%, 1%, 2%, 3%, 5%, 7%, 10%, 13%, 17%, 21%, 26%, 31%, 37%, 43%, 50%, 57%, 65%, 73%, 82%, 91%, and 99.9%. Figure 4 shows the performance of Eq. (17) for different porosity values, which verifies the accuracy of the equations. The calculated values almost always fell on the line 45°, and it is evident that the porosity values calculated using Eq. (17) were highly consistent with the true porosity values. In addition, Fig. 4 shows the relative errors of the calculated porosity values, which indicate that the relative error between the calculated and real porosities was less than 2% when the porosity values exceeded 10%. Further, the absolute error of porosity was less than 0.1% when the porosity values were less than 10%.

If $\left(L^{\mathrm{el}}_{E_0-E_1}\right)^2$ in Eq. (11) is neglected, the slowing-down length can be described as $L_f = \sqrt{\frac{\ln\left(\frac{E_0}{E_1}\right)}{3\zeta\Sigma^2_{\mathrm{in}}} + \frac{\ln\left(\frac{E_1}{E_t}\right)}{3\zeta\Sigma^2_{\mathrm{el}}}}$. Thus,

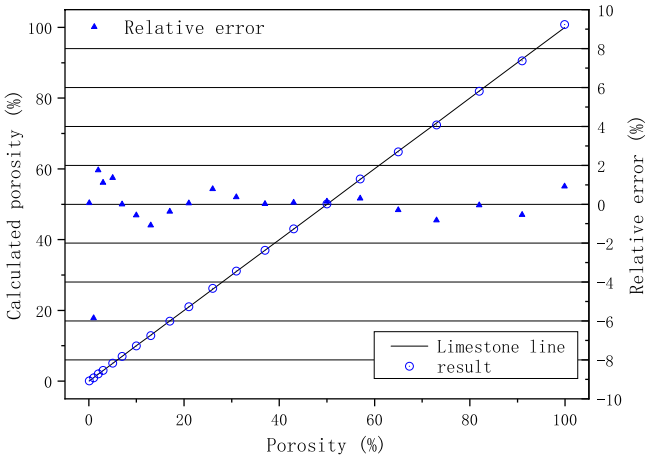

Fig. 4 (Color online) Results of porosity and error determined by Eq. (17)

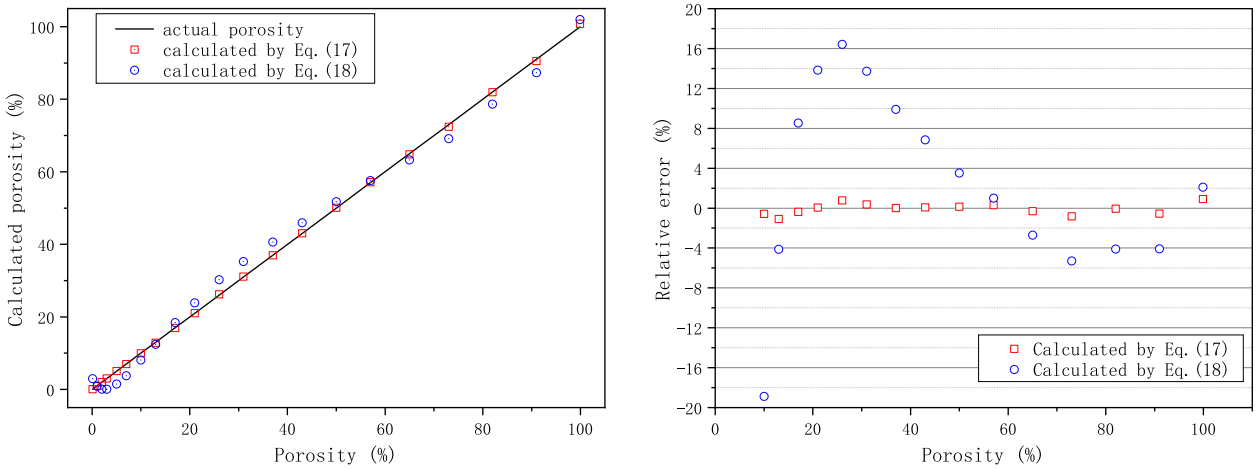

Fig. 5 (Color online) Comparison of the results calculated by Eqs. (17) and (18). **a** Calculated porosity and **b** relative error

Eq. (17) is simplified and the algorithm of the model can be obtained as follows:

$$\phi = 1.768 \times \frac{\ln\left(0.811 \times R_t\right)^2}{\rho} - 0.000176 \tag{18}$$

Figure 5 presents a comparison of the results calculated using Eqs. (17) and (18). As evident, the porosity values calculated using Eqs. (17) and (18) were consistent with the actual porosity values shown in Fig. 5a. Figure 5b shows a comparison of the relative errors obtained using Eqs. (17) and (18) when the porosity values exceeded 10%. Compared with Eq. (17), the relative error of Eq. (18) was larger, particularly at low porosities. Table 2 indicates that the absolute error reached 3.6%. for Eq. (18), because the actual porosity was less than 7%. This demonstrates that the influence of elastic scattering from E_0 to E_1 on the porosity measurement cannot be ignored.

Table 2 Absolute error of porosity by Eqs. (17) and (18)

Actual porosity (%)	Calculated porosity (%)		Absolute error of porosity (%)	
	By Eq. (17)	By Eq. (18)	By Eq. (17)	By Eq. (18)
0.1	0.1001	2.9772	0.0001	2.8772
1	0.9415	0.9240	− 0.0585	− 0.0760
2	2.0351	0.0657	0.0351	− 1.9343
3	3.0332	0.0503	0.0332	− 2.9497
5	5.0675	1.4789	0.0675	− 3.5211
7	6.9933	3.8063	− 0.0067	− 3.1937

4.3 Influence of density accuracy on porosity measurement

The relationship between density and porosity can be observed from Eqs. (12) and (16). As evident, as the density decreases, the porosity tends to increase. The introduction of density correction has resulted in problems in the accuracy of porosity measurements caused by density measurements. In conventional density measurements, the measurement error, $\Delta\rho$, should generally be less than 0.015 g/cm^3. To evaluate the effect of density precision on the neutron porosity measurement, the calculated results were obtained as shown in Fig. 6 and Table 3 for density errors of +0.015 g/cm^3 and −0.015 g/cm^3.

As shown in Fig. 6 and Table 3, the absolute error between the calculated and actual porosities was less than 0.3% when the actual porosity was below 7%. Further, the relative error was less than 4% in areas where the actual porosity was above 7%. In particular, when the porosity exceeded 2%, the relative error was less than 30%. As the porosity increased, the relative error gradually decreased. Therefore, the measurement error of the density exerts a minimal effect on the porosity in conventional density measurements.

This method considers the nonlinear relationship between the detector count and porosity and density during the transport of D–T neutrons in the formation, indicating that the proposed algorithm can effectively improve the measurement accuracy of the porosity compared with the existing density correction algorithm. Further, it greatly eliminates the influence of density measurement error in the actual measurement process.

Table 3 Absolute error of porosity with a density error of ± 0.015 g/cm^3

Actual porosity (%)	Actual density (g/cm^3)	Absolute error of porosity (%)	
		Density error +0.015 g/cm^3	Density error −0.015 g/cm^3
0.1	2.7013	0.00006	0.00006
1	2.68597	− 0.10158	− 0.01522
2	2.66894	− 0.05899	0.12956
3	2.65191	− 0.10247	0.16961
5	2.61785	− 0.14223	0.27824
7	2.58379	− 0.27453	0.26220

5 Conclusion

The fast neutron slowing-down length of the D–T source is affected by both elastic and inelastic scattering. A slowing-down model for fast neutrons was established to explain the process of neutron slowing-down. In this model, the contribution of elastic scattering to the slowdown of neutrons was considered to above the threshold of inelastic scattering. The model shows that the slowing-down length of the D–T neutrons comprised $L^{\text{in}}_{E_0-E_1}$, $L^{\text{el}}_{E_0-E_1}$ and $L^{\text{el}}_{E_1-E_t}$. Further analysis indicated that for a relatively low porosity of the formation, the probability of neutrons slowing-down through inelastic scattering was higher. As the porosity increased, the probability of inelastic scattering decreased. However, owing to the rapid increase in the elastic scattering macroscopic cross section, the contribution of inelastic scattering to the slowing-down length became significant. The results also indicated that if elastic scattering was ignored above the inelastic

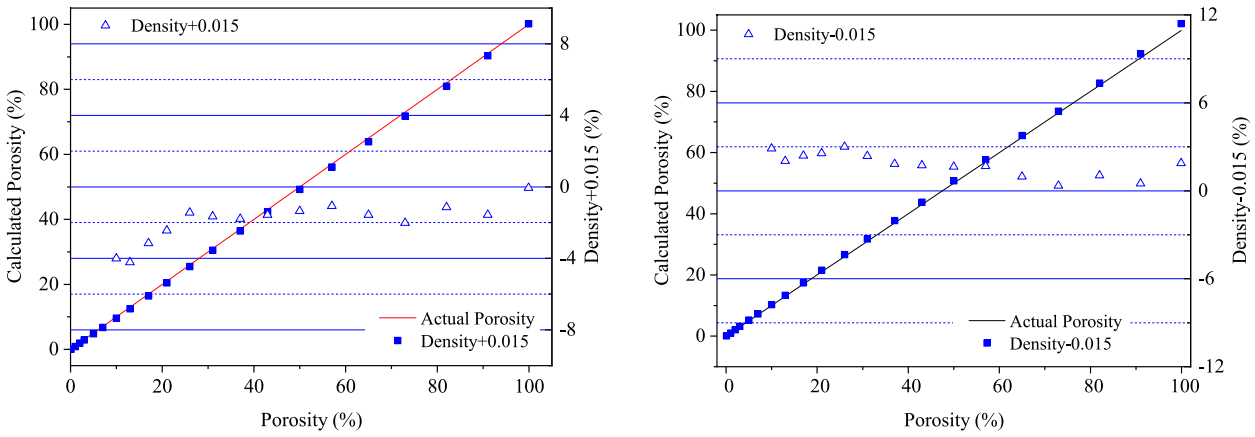

Fig. 6 (Color online) Effects of density on porosity for density error of **a** +0.015 g/cm^3 and **b** −0.015 g/cm^3

scattering threshold energy, it would exert an impact of approximately 4% on the slowing-down length of neutron elastic scattering. Further, this exceeded the accuracy for porosity measurement. Therefore, the effect of elastic scattering cannot be ignored at the high energy in the porosity measurement. Based on the slowing-down model, a porosity density correction algorithm was developed to improve the porosity sensitivity of D–T neutrons. The algorithm was a complex function of density and porosity and cannot be simply written as $f(\rho)g(\phi)$.

Finally, a porosity logging model was created using TopMC/SuperMC, and the effectiveness of the established algorithm was verified through simulations. The results showed that the relative error between the calculated and actual porosities was less than 2% when the porosity values exceeded 10%, whereas the absolute error of the porosity was less than 0.1% when the porosity values were less than 10%. If $L^{\mathrm{el}}_{E_0-E_1}$ was ignored, the relative error in porosity reached 19%. The comparison showed that the elastic scattering of high-energy neutrons exerted a significant influence on the measurement accuracy of the porosity.

In addition, the effect of density precision on porosity measurement was evaluated. The calculated results showed that the absolute error was less than 0.3% when the actual porosity was below 7%. Further, the relative error was less than 4% in areas where the actual porosity was above 7%.

The algorithm, proposed through theoretical deduction based on the case of a fixed lithology and distance between the detector and neutron source, can improve the overall measurement accuracy of the density correction method. Regarding the use of D–T neutron sources for porosity measurements, this study provides certain reference values.

This study was primarily conducted using simulation instruments in a standard well. In the future, scaling and tests can be conducted based on actual instruments, and further analysis of the influencing factors of complex environments, particularly the influence of lithology and wellbore diameter, will be conducted.

Acknowledgements This study was based on a TopMC/SuperMC simulation of the described model. This study received strong support from other members of the FDS Consortium.

Author contributions All authors contributed to the study conception and design. Material preparation, data collection and analysis were performed by S-HZ, Y-LT, BC, L-JH, J-QJ, Y-ZL, FW and QG. The first draft of the manuscript was written by S-HZ, and all authors commented on previous versions of the manuscript. All authors read and approved the final manuscript.

Data availability The data that support the findings of this study are openly available in Science Data Bank at https://cstr.cn/31253.11.sciencedb.j00186.00541 and https://doi.org/10.57760/sciencedb.j00186.00541.

Declarations

Conflict of interest The authors declare that they have no conflict of interest.

References

1. T. Gjerdingen, J. Hilton, N. Bounoua et al., Sourceless LWD porosity determination: a fit for purpose formation evaluation with significant HS & E benefits, in *SPE Annual Technical Conference and Exhibition. Society of Petroleum Engineers* (2012). https://doi.org/10.2118/159522-MS
2. J.D. Aitken, R. Adolph, M. Evans et al., Radiation sources in drilling tools: comprehensive risk analysis in the design, development and operation of LWD tools, in *SPE International Conference on Health, Safety and Environment in Oil and GasExploration and Production*, March 20–22 (2002). https://doi.org/10.2118/73896-MS
3. A. Badruzzaman, S. Bames, F. Bair et al., Radioactive sources in petroleum industry: applications, concerns and alternatives, in *AsiaPacific Health, Safety, Security and Environment Conference*, 4–6 (2009). https://doi.org/10.2118/123593-MS
4. Non-isotopic alternative technologies working group, *Non-radioisotopic Alternative Technologies White Paper* (U.S. Department of Homeland Security Cybersecurity and Infrastructure Security Agency, 2019)
5. F. Zhang, C. Yuan, Monte Carlo simulation on compensated neutron porosity logging with D–D neutron porosity logging with D–D neutron generator. Well Logging Technol. **34**(3), 227–232 (2010). https://doi.org/10.16489/j.issn.1004-1338.2010.03.004. (**in Chinese**)
6. Y. Yan, B.Y. Li, S.P. Zheng et al., Monte Carlo simulation of the neutron porosity logging using D–D neutron generator. J. Lanzhou Univ. (Nat. Sci.) **48**(03), 123–127 (2012). https://doi.org/10.13885/j.issn.0455-2059.2012.03.009. (**in Chinese**)
7. A. Badruzzaman, A. Schmidt, A. Antolak et al., Neutron generator as alternatives to Am–Be source in well logging: an assessment of fundamentals. Petrophysics **60**(1), 136–170 (2019). https://doi.org/10.30632/PJV60N1-2019a10
8. L. Bond, K. Denslow, J. Griffin et al., *Evaluation of Non-nuclear Techniques for Well Logging Technology Evaluation* (PNNL, Washington, 2010). https://doi.org/10.2172/1006309
9. J. Griffin, T. Moran, L. Bond, *Radiation Source Replacement Workshop* (PNNL, Washington). https://doi.org/10.2172/1062523
10. G. Weller, R. Griffiths, C. Stoller et al., A new integrated LWD platform brings next-generation formation evaluation services. In *SPWLA46thAnnual Logging Symposium* (Society of Petrophysicists and Well-Log Analysts, Louisiana, USA, 2005)
11. D.V. Ellis, J.M. Singer, *Well Logging for Earth Scientists* (Inc, New York, 2007), pp.383–413. https://doi.org/10.1007/978-1-4020-4602-5_15
12. H. Guo, K. Zhao, N. Lu et al., The design of "multiple energies from one source'' in D–T neutron tube. Nucl. Sci. Tech. **27**(05), 127–132 (2016). https://doi.org/10.1007/s41365-016-0119-1
13. A. Badruzzaman, A. Schmidt, A. Antolak, An assessment of fundamentals of neutron porosity interpretation: americium–beryllium source versus neutron generator-based alternatives, in *SPWLA 58th Annual Logging Symposium* (Society of Petrophysicists and Well-Log Analysts, Oklahoma, USA, 2017)
14. F. Zhang, X. Jin, S. Hou, Monte Carlo simulation on compensated neutron porosity logging in LWD with D–T pulsed neutron generator. J. Isot. **23**, 15–21 (2010). https://doi.org/10.7538/tws.2010.23.01.0015. (**in Chinese**)

15. H. Yu, Y. Zhou, X. Chen et al., Analysis of factors affecting the sensitivity of neutron porosity logging. Nucl. Tech. **41**, 53–58 (2018). https://doi.org/10.11889/j.0253-3219.2018.hjs.41.020502. (**in Chinese**)
16. Y. Ge, Q. Luo, H. Chen et al., A new porosity evaluation parameter based on neutron porosity logging. Appl. Radiat. Isot. **190**, 110481 (2022). https://doi.org/10.1016/j.apradiso.2022.110481
17. J. Liu, F. Zhang, R.P. Gardner et al., A method to improve the sensitivity of neutron porosity measurement based on D–T source. Nat. Gas Sci. Eng. **33**, 879–884 (2016). https://doi.org/10.1016/j.jngse.2016.06.028
18. W. Wu, H. Wang, H. Wang et al., Formation density affects and corrections in pulsed neutron porosity logging. Nucl. Tech. **41**, 80406 (2018). https://doi.org/10.11889/j.0253-3219.2018.hjs.41.080406. (**in Chinese**)
19. N. Yang, Data correction and experimental study of neutron porosity logging using D–T source. Nucl. Tech. **43**, 90–94 (2020). https://doi.org/10.11889/j.0253-3219.2020.hjs.43.040502. (**in Chinese**)
20. H. Wang, A. Yue, X. Zhang et al., Study on density correction of pulsed neutron porosity logging. Well Logging Technol. **45**, 552–556 (2021). https://doi.org/10.16489/j.issn.1004-1338.2021.06.002. (**in Chinese**)
21. S. Fricke, D.P. Madio, B. Adolph et al., Thermal neutron porosity using pulsed neutron measurements, in *SPWLA*49th*Annual Logging Symposium* (Society of Petrophysicists and Well-Log Analysts, Edinburgh, Scotland, 2008)
22. H. Yu, Z. Wang, Z. Xue et al., Corrections of fast neutron inelastic scattering effects on D–T neutron porosity logging. Appl. Radiat. Isot. **190**, 110486 (2022). https://doi.org/10.1016/j.apradiso.2022.110486
23. K.H. Beckurts, K. Wirtz, *Neutron Physics*, 1st edn. (Springer, New York, 1964), pp.121–123
24. M.B. Chadwick, M. Herman, P. Obložinský et al., ENDF/B-VII.1 nuclear data for science and technology: cross sections, covariances, fission product yields and decay data. Nucl. Data Sheets **112**(12), 2887–2996 (2011)
25. Y. Wu, Multifunctional neutronics calculation methodology and program for nuclear design and radiation safety evaluation. Fusion Sci. Technol. **74**, 321–329 (2018). https://doi.org/10.1080/15361055.2018.1475162
26. D. McKeon, H. Scott, SNUPAR-a nuclear parameter code for nuclear geophysics applications. IEEE Trans. Nucl. Sci. **36**, 1215–1219 (1989). https://doi.org/10.1109/23.34634
27. Y. Qiu, L. Xia, H. Peng et al., On benchmark verification of MCNP modeling in compensated neutron logging. Well Logging Technol. **28**, 471–477 (2004). https://doi.org/10.16489/j.issn.1004-1338.2004.06.001. (**in Chinese**)
28. Y. Zhou, H. Yu, M. Wang et al., Numerical simulation of controllable source neutron porosity logging based on CLYC detector. Nucl. Tech. **44**, 74–79 (2021). https://doi.org/10.11889/j.0253-3219.2021.hjs.44.040501. (**in Chinese**)
29. H. Yu, H. Xiao, Monte Carlo study on shielding of D–T neutron porosity logging-while-drilling tool. Nucl. Electron. Detect. Technol. **33**, 1123–1126 (2013). https://doi.org/10.3969/j.issn.0258-0934.2013.09.020. (**in Chinese**)
30. P. Parvaresh, M. Sohrabpour, Design and testing of a neutron porosity probe using MCNP code. J. Radioanal. Nucl. Chem. **260**(2), 335–337 (2004). https://doi.org/10.1023/b:jrnc.0000027106.91120.1a
31. R.C. Little, M. Mickael, K. Verghese et al., Benchmark neutron porosity log calculations: a comparison of MCNP and the specific purpose code McDNL. IEEE Trans. Nucl. Sci. **36**(1), 1223–1226 (1989). https://doi.org/10.1109/23.34636
32. L. Zhang, H. Yu, Y. Li et al., Improved formation density measurement using controllable D-D neutron source and its lithological correction for porosity prediction. Nucl. Sci. Tech. **33**(01), 26–36 (2022). https://doi.org/10.1007/s41365-022-00988-1